Electrical conductivity in texturally equilibrated fluid-bearing forsterite aggregates at 800 ºC and 1 GPa: implications for the high electrical conductivity anomalies in mantle wedges

Yongsheng Huang[1*], Haihao Guo[2], Takayuki Nakatani[1, a], Kentaro Uesugi[3], Michihiko Nakamura[1], Hans Keppler[2]

1. *Department of Earth Science, Graduate School of Science, Tohoku University, Aramaki-Aza-Aoba, Aoba-ku, Sendai, Miyagi 980-8578, Japan*

2. *Bayerisches Geoinstitut, University of Bayreuth, 95440 Bayreuth, Germany*

3. *Spring-8, Japan Synchrotron Radiation Research Institute (JASRI), 1-1-1, Kouto, Sayo-cho, Sayo-gun, Hyogo 679-5198 Japan*

a. *Current address: Geological Survey of Japan, AIST Central 7, Higashi 1-1-1, Tsukuba, Ibaraki 305-8567, Japan*

* Corresponding Author Email: huang.yongsheng.e1@tohoku.ac.jp

Key points

1. Electrical conductivity in texturally equilibrated brine-bearing forsterite aggregates was measured at 800 °C and 1 GPa by a novel setup.

2. 3-D images were obtained by synchrotron X-ray CT to precisely determine the fluid fractions and to visualize the fluid distribution.

3. Above 1.0 vol.% fluid with 5 wt.% NaCl is required to explain the high conductivity anomalies above 0.01 S/m in deep fore-arc mantles.

Abstract

Aqueous fluids are one of the principal agents of chemical transport in Earth´s interior. The precise determination of fluid fractions is essential to understand bulk physical properties, such as rheology and permeability, and the geophysical state of the mantle. Laboratory-based electrical conductivity measurements are an effective method for estimating the fluid distribution and fraction in a fluid-bearing rock. In this study, the electrical conductivity of texturally equilibrated fluid-bearing forsterite aggregates was measured for the first time with various fluid fractions at a constant salinity of 5.0 wt.% NaCl at 1 GPa and 800 °C. We found that the electrical conductivity nonlinearly increases with increasing fluid fraction, and the data can be well reproduced by the modified Archie's law. The three-dimensional (3-D) microstructure of the interstitial pores visualized by the high-resolution synchrotron X-ray computed micro-tomography (CT) shows a change in fluid distribution from isolated pockets at a fluid fraction of 0.51 vol.% to interconnected networks at fluid fractions of 2.14 vol.% and above due to grain anisotropy and grain size differences, accounting for the nonlinear increase in electrical conductivity. The rapid increase in conductivity indicates that there is a threshold fluid fraction between 0.51 and 2.14 vol.% for forming interconnected fluid networks, which is consistent with the 3-D images. Our results provide direct evidence that the presence of > 1.0 vol.% aqueous fluid with 5.0 wt.% NaCl is required to explain the high conductivity anomalies above 0.01 S/m detected in deep fore-arc mantle wedges.

Plain Language Summary

Aqueous fluids are one of the principal agents for transporting material in the Earth's interior. Electrical conductivity measurements can be used to reveal the distribution of water in the Earth´s mantle because the presence of a water-rich fluid in a rock can significantly enhance the bulk conductivity. To better constrain the fluid distribution and fraction in mantle wedges, we measured the electrical conductivity of olivine containing minor amounts of a salt-bearing aqueous fluid at high pressure and temperature. The three-dimensional microstructure of the interstitial pores visualized by the high-resolution synchrotron X-ray computed micro-tomography shows that the fluid distribution changes from isolated pockets to interconnected networks with increasing fluid fraction, accounting for the observed nonlinear increase in electrical conductivity. Our results provide direct evidence that the presence of > 1.0 vol.% aqueous fluid with 5.0 wt.% NaCl is required to explain the high conductivity anomalies detected in deep fore-arc regions.

Key words: Electrical conductivity; Brine-bearing forsterite aggregates; Textural equilibrium; X-ray CT; Mantle wedge; Subduction zones.

1. Introduction

In subduction zones, aqueous fluids released from the subducting slab percolate through the mantle wedge, controlling arc magma genesis and element recycling (e.g., Hermann et al., 2006; Iwamori, 1998; van Keken et al., 2011; Tatsumi, 1986). Because the presence of fluid significantly enhances the bulk electrical conductivity of rocks (e.g., Guo et al., 2015; Shimojuku et al., 2012, 2014; Sun et al., 2020), the distribution of fluids in subduction zones may be imaged by magnetotelluric (MT) observations. Recently, a growing number of MT observations have revealed high electrical conductivity anomalies (0.001–1 S/m) in the deep fore-arc crusts and mantle wedges in some subduction zones (e.g., Araya Vargas et al., 2019; Pommier & Evans, 2017; Worzewski et al., 2011). Because the temperature is relatively low in fore-arc regions (<700–800 °C, Syracuse et al., 2010), aqueous fluid rather than silicate melt has been assumed to be the highly conductive phase present in the lower crust and mantle wedge, supplied by the subducting slab through a permeable window in the fore-arc mantle wedge (Huang et al., 2019). Although conductive minerals such as sulfide (Ducea & Park, 2000), graphite (Frost et al., 1989; Glover, 1996), and magnetite (Manthilake et al., 2016) have also been suggested to be the cause of the observed high electrical conductivity, their volume fraction may not be sufficiently high to form interconnected networks in rocks.

Fluid fraction is a key parameter that controls not only the electrical conductivity, but also other physical properties of fluid-bearing rocks, such as rheology, permeability, and seismic wave velocities (Bloch et al., 2018; Rippe et al., 2013; von Bargen & Waff, 1986; Worzewski et al., 2011). The accurate quantitative estimation of the fluid fraction, therefore, is fundamentally important to better interpret geophysical anomalies and to understand the dynamics of material cycling in subduction zones. A number of models with homogeneous and simple fluid geometries have been proposed to describe the fluid fraction dependence of electrical conductivity in fluid–rock mixtures (Archie's law, Archie, 1942; modified Archie's law, Glover et al., 2000; Hashin-Shtrikman upper and lower bound model (HS model), Hashin & Shtrikman, 1962; tube model, Schmeling, 1986; cube model, Waff, 1974). In the

cube and HS upper bound models, all grain boundaries are assumed to be completely wetted by a fluid phase. In the tube model, the fluid forms an interconnected tube network at grain edges, and Archie's law is empirical and has been utilized to describe fluid distribution in porous water-saturated sandstone, allowing change in fluid connectivity with increasing fluid fraction (e.g., ten Grotenhuis et al., 2005).

At high pressure (P)–temperature (T) conditions, the equilibrium fluid distribution is primarily controlled by the dihedral angle (i.e., wetting angle) between the rock matrix and aqueous fluid. In an ideal system with isotropic interfacial energy and uniform grain size, the system has one true dihedral angle accompanied by curved solid-fluid interfaces with constant mean curvature, and the fluid distribution is homogenous. The fluid forms an interconnected network at all grain edges, as in the tube model, for a dihedral angle below the critical value of 60°. For higher dihedral angles, the fluid fills isolated pockets and a relatively high fluid fraction is required to form interconnected fluid networks (Watson & Brenan, 1987; Holness, 1992, 1993). In reality, however, minerals have anisotropic interfacial energies; thus, the system has a range of true dihedral angles associated with crystallographically controlled faceted interfaces. Pores surrounded by facetted planes can result isolated fluid pockets at grain corners even at dihedral angles smaller than 60°(e.g., Price et al., 2006), affecting the bulk fluid connectivity of the system. In addition, based on the grain size distribution in real rocks, fluid may concentrate in the domains of smaller grains (Wark & Watson, 2000). Therefore, the fluid distribution in a fluid-bearing, deep-seated rock may deviate from the ideal systems, preventing a precise evaluation of the fluid fraction from MT data using simple theoretical models. Experimental measurements of the electrical conductivity in texturally equilibrated fluid-bearing rocks are necessary to constrain the actual relationship between electrical conductivity and fluid fraction.

In the last decade, many laboratory-based electrical conductivity measurements have been conducted in fluid-bearing systems (e.g., Guo & Keppler, 2019; Guo et al., 2015; Shimojuku et al., 2012, 2014; Sun et al., 2020). For example, Shimojuku et al. (2012, 2014) measured the electrical conductivity of a fluid-bearing quartzite as a function of fluid fraction and fluid salinity, and suggested that a high fluid fraction above 32.0 vol.% or a high salinity above 10.0 wt.% is required to account for high conductivity anomalies in the lower crust. However, these measurements were performed with short run durations at constant P–T; thus, the attainment of textural equilibrium was not guaranteed, similar to other previous

experiments. Olivine is the dominant mineral in mantle wedges, while previous studies utilized quartz (Shimojuku et al., 2012 and 2014), albite (Guo et al., 2015), and clinopyroxene (Sun et al., 2020) as the matrix mineral, which may affect the dihedral angle (i.e., fluid geometry) and fluid chemistry (i.e., charge carriers in the fluid) in the experimental systems. In addition, the lack of the three-dimensional (3-D) analyses of the fluid fraction and pore structures in previous experiments hampers the accurate interpretation of MT data due to an insufficient physical understanding of the fluid fraction dependence of electrical conductivity.

In this study, we measured the electrical conductivity in texturally equilibrated H_2O–NaCl-bearing forsterite (Mg-endmember of olivine) aggregates with various fluid fractions at a NaCl concentration of 5.0 wt.% at 800 °C and 1 GPa. Combined with 3-D images of the fluid distribution determined by synchrotron X-ray computed micro-tomography (CT), the results are used to discuss the fluid fraction dependence of electrical conductivity and estimate the fluid fraction in mantle wedges.

2. Experimental procedures

2.1. Sample preparation

To avoid the difficulties associated with electrical conductivity measurements in iron-bearing systems, synthetic forsterite was used as the starting material. Polycrystalline forsterite aggregates were synthesized from iron-free gel powder at 1200 °C and 1.8 GPa in a piston cylinder apparatus with 1/2-inch diameter talc-pyrex assemblies at Bayerisches Geoinstitut, University of Bayreuth. Details of the sol-gel preparation are described in Ohuchi and Nakamura (2006). The gel powders were placed in an oven at 300 °C for 12 h to remove moisture, and were then loaded in a platinum capsule (outer diameter: 5.0 mm) that was sealed by arc welding. The piston cylinder apparatus was first pressurized up to 90% of the target pressure; then, the remaining pressure was applied after heating to the target temperature. During the run, the temperature was monitored and controlled by an S-type thermocouple ($Pt–Pt_{90}Rh_{10}$). The experiment duration was 24 h at the target temperature. The experiments were quenched to room temperature within 1 min, and the pressure was released slowly. The run products were extracted from the platinum capsules and checked under an optical microscope. The synthesized forsterite grains were then ground in an agate mortar and were sieved to obtain size fractions of 38–53 μm. Moreover, reagent-grade NaCl (Chem.

Pure, 99.999% purity) was dissolved in deionized and distilled water under ambient conditions to obtain a solution with a salinity of 5.0 wt.%.

2.2. Electrical conductivity measurements

Electrical conductivity measurements were conducted at 800 °C and 1.0 GPa in a piston cylinder apparatus with 3/4-diameter talc-pyrex assemblies at Bayerisches Geoinstitut, University of Bayreuth. The configuration of the cell assemblies was as described by Guo and Keppler (2019). A 1-mm diameter platinum rod and a $Pt_{95}Rh_5$ capsule with an outer diameter of 5.0 mm and inner diameter of 4.4 mm were employed as the inner and outer electrodes, respectively (Figure 1). A ceramic disk with 1 mm thickness was placed at the bottom of the $Pt_{95}Rh_5$ capsule. The forsterite powder and saline fluid of each experiment (initial fluid fractions: 0.5 wt.%, 2.5 wt.%, 5.0 wt.% and 10.0 wt.%) were loaded into the capsule between two alumina disks with 1-mm-diameter holes containing the platinum rod inner electrode. A boron nitride disk at the end of the capsule provided the seal. A thin ceramic Al_2O_3 tube tightly fitted around the Pt rod and the central hole of the $Pt_{95}Rh_5$ lid was served as an insulator. Two Pt wires with a diameter of 0.35 mm were welded to the inner and outer electrodes and connected to a Solartron 1260 impedance analyzer for measuring the conductivity. The whole capsule was surrounded by another shell of boron nitride to improve sealing. The procedures for increasing temperature and pressure were the same as described above. The experiments were conducted at 800 °C and 1 GPa for 8 days, and the impedance spectra were measured every day using an alternating current voltage of 500 mV sweeping from 10 MHz to 1 Hz.

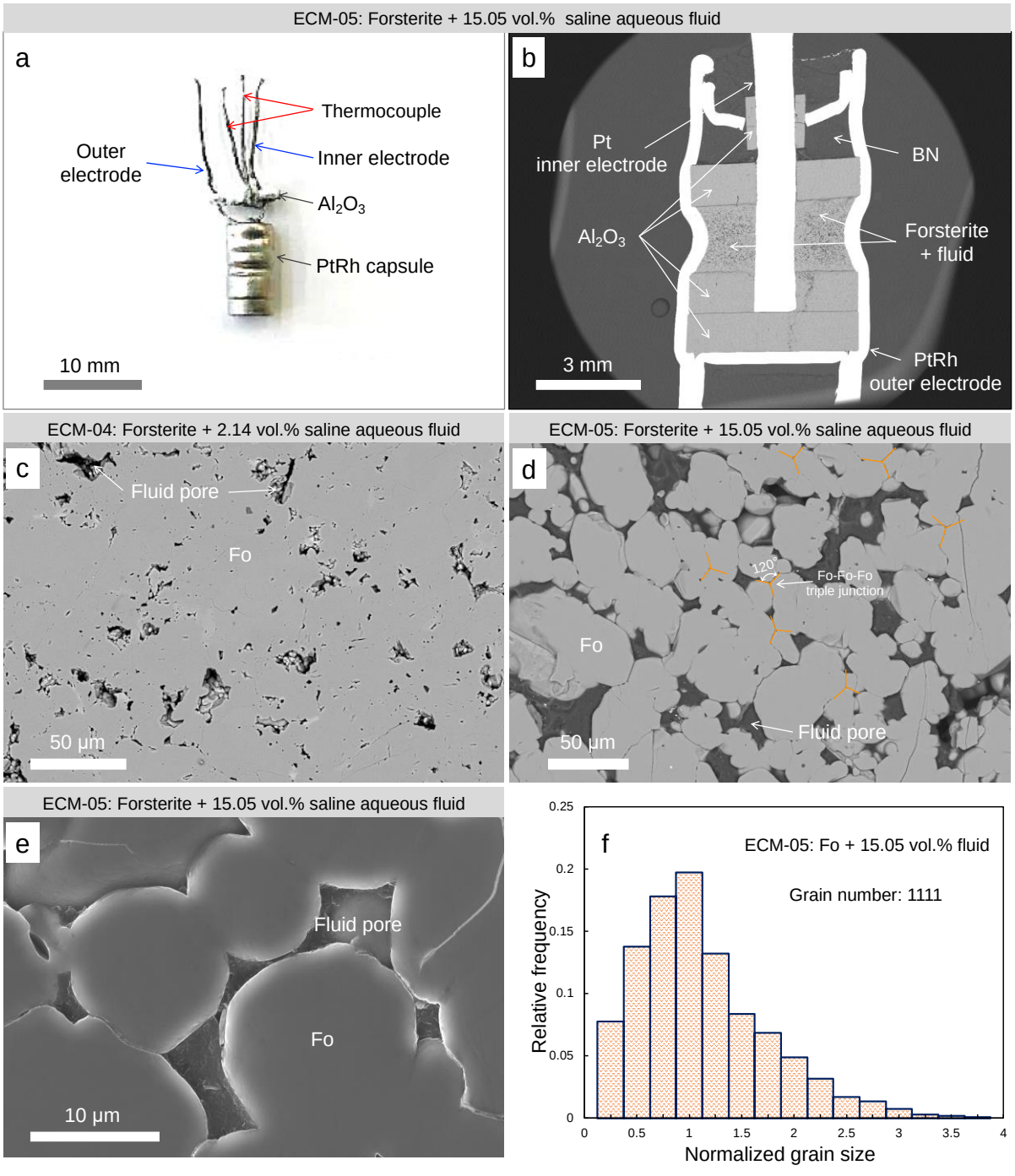

Figure 1. Sample characterization. **(a)** Capsule recovered after an electrical conductivity measurement with a final fluid fraction of 15.05 vol.%. **(b)** Representative backscattered electron (BSE) image of the cross section of the recovered capsule with a final fluid fraction of 15.05 vol.%. **(c)** BSE image of the recovered sample with a final fluid fraction of 2.14 vol.%. **(d)** BSE image of the recovered sample with a final fluid fraction of 15.05 vol.%. The fluid pores were filled with epoxy resin during sample preparation. The orange marks represent the forsterite-forsterite-forsterite triple junctions with intersection angles of ~120°, suggesting the attainment of textural equilibrium. **(e)** Secondary electron (SE) image of the recovered sample with a final fluid fraction of 15.05 vol.%, showing small dihedral angles between forsterite grains and fluids. **(f)** Representative histogram of the grain size distribution, normalized by the mean grain size of the recovered sample with a final fluid fraction of 15.05 vol.%. The grain size is concentrated with a peak around the mean grain size. Abbreviation: Fo = forsterite.

The bulk conductivity (σ_b) of the whole cell was calculated from the resistance and the dimensions of the cell, using the equation for the cell constant in cylindrical geometry:

$$\sigma_b = \frac{\ln(r_o/r_{i)}}{2\pi lR}, \qquad (1)$$

where the cylindrical electrodes have an outer radius r_o, and inner radius r_i, l is the length of the sample, and the measured electrical resistance is R. The electrical conductivities measured in this study were usually very high so that the background conductivity of assemblies was negligible for all investigated systems (Guo & Keppler, 2019; Ni et al., 2011). The two-electrode method employed in this study requires a correction for the resistance of the electrode wires sample if the measured resistance of the sample is very low (Pommier et al., 2010). We utilized the short-circuit method introduced by Ni et al. (2011) to correct our measured data.

2.3. Scanning electron microscope (SEM) observations

The experiments were immediately quenched to room temperature at the end of experimental run within 1 min by turning off the heating power after the last electrical conductivity measurement. The recovered capsules were cut open using a diamond wire saw to expose the run products. The run products were then impregnated with epoxy resin in a vacuum box and polished down to 1.0 μm surface roughness with alumina powder and subsequently to 0.06 μm by colloidal silica suspension. The polished cross sections were observed using a field emission-type SEM (FE-SEM; JEOL JSM-7100F) with an accelerating voltage of 15 keV. The dimensions of the samples (i.e., outer radius r_o, inner radius r_i, and length l) were carefully measured in backscattered electron (BSE) images.

2.4. Synchrotron X-ray microtomography

In order to determine the fluid distribution and fraction, the recovered samples were prepared for X-ray CT analysis with synchrotron radiation. Microtomography of run products was conducted at the undulator beam line BL20XU at the Spring-8 facility, Hyogo, Japan. The cross-section of the monochromatic X-ray beam was approximately 2 mm ×1 mm at 240 m from the light source (around the sample position). The highly collimated undulator radiation from the low emittance storage ring used in this study is very suitable for high spatial resolution tomography. The undulator gap (K-value) was properly tuned at each

energy to obtain a relatively large field of view in the vertical direction; that is, the selected energy was slightly lower than the odd-order peaks of the undulator radiation. Therefore, the flux density of the monochromatic beam was approximately 5×10^{12} photons s^{-1} mm^{-2} (Uesugi et al., 2001) at the sample position. The contrast resolution of the X-ray CT system in SPring-8 has been reported by Uesugi et al. (1999). For each recovered sample, around 1,800 CT images were taken by X-ray CT, and a considerable sub-volume of the run products was extracted from these images, avoiding any cracks, to precisely evaluate the fluid fraction.

2.5. Determination of water content

The water content in the forsterite aggregate of one recovered sample (Sample No. ECM-3) was measured using a Thermo Scientific Nicolet iN10 FT-IR Microscope (FTIR) at Tohoku University. A doubly polished section of the sample, with a thickness of ~300 μm, was prepared for the FT-IR measurement. The unpolarized infrared spectra of the sample were obtained from 17 sampling points. At several points measurements were carried out with either increasing aperture size (from 50 × 50 to 400 × 400 μm) or scanning time (from 3 to 25 s), to evaluate the influence of aperture size or scanning time on measured content. Then 10 sampling points were measured with a constant aperture size of 200 × 200 μm and scanning time of 12 s. The water content was calculated from the average of the measured absorbance, using the integrated extinction coefficients of Bell et al. (2003) and an orientation factor of 1/3.

3. Results

3.1. Micro-textures and fluid fractions of the recovered sample

The run products are composed of sintered aggregates of forsterite and interstitial pores, which were occupied by saline aqueous fluid (Figure 1). Textural maturation was well established within the run duration of 8 days. The presence of many forsterite triple junctions with angles of ~120° (Figure 1-d) indicates the attainment of balance of interfacial tensions at triple junctions (Huang et al., 2020; Liu et al., 2018). The grain size distribution determined from BSE images by Image-J shows a narrow grain size distribution with a peak around the mean grain size (Figure 1-f), in agreement with textural equilibrium (Faul, 1997; ten Grotenhuis et al., 2005). A thin reaction layer with a thickness of less than 100 μm was observed between the forsterite and the Al_2O_3 disk. Although this layer contains interstitial

pyroxene along with relict olivine, its influence on the bulk electrical conductivity should be negligible, as all these phases are Fe-free and therefore poor conductors (e.g., Dai & Karato, 2009).

The fluid fractions of the experiments were precisely determined using the 3-D images that were obtained from synchrotron X-ray CT of the run products. The fluid fractions of the samples before and after electrical conductivity measurement are shown in the Table 1. Representative 3-D images of the sub-volumes of the recovered samples are shown in the Supporting Information Figure S1. The fluid fraction in the recovered samples is always smaller than the initial fluid fraction, with the difference being up to 12.37 vol.%. Although the initial fluid fraction was precisely controlled, the fluid loss at high P–T conditions was inevitable because of the initially imperfect sealing of the experimental setup, especially during the first day. After this period, the fluid fraction likely remained constant, as discussed below, based on the time-series electrical conductivity data (Figure 2). The fluid fractions estimated from the recovered samples represent the fluid fractions during the last measurements of electrical conductivity.

Table 1. Summary of experimental conditions and results.

Run No.	T (°C)	P (GPa)	wt.% of fluid (before EC)	vol.% of fluid (before EC)	vol.% of fluid (after EC)	Salinity (wt.%)	σ (s/m)	logσ (S/m)
ECM-6	800	1	0.50	1.7(0.1)	0.51(0.05)	5.00	1.65E-03	-2.78
ECM-4	800	1	2.50	8.0(0.1)	2.14(0.05)	5.00	3.56E-02	-1.45
ECM-3	800	1	5.00	15.2(0.1)	8.14(0.05)	5.00	2.41E-01	-0.62
ECM-5	800	1	10.00	27.4(0.1)	15.05(0.05)	5.00	4.80E-01	-0.32

Note: The volume fractions of fluid after the experiments were determined from the recovered samples by using synchrotron X-ray CT.

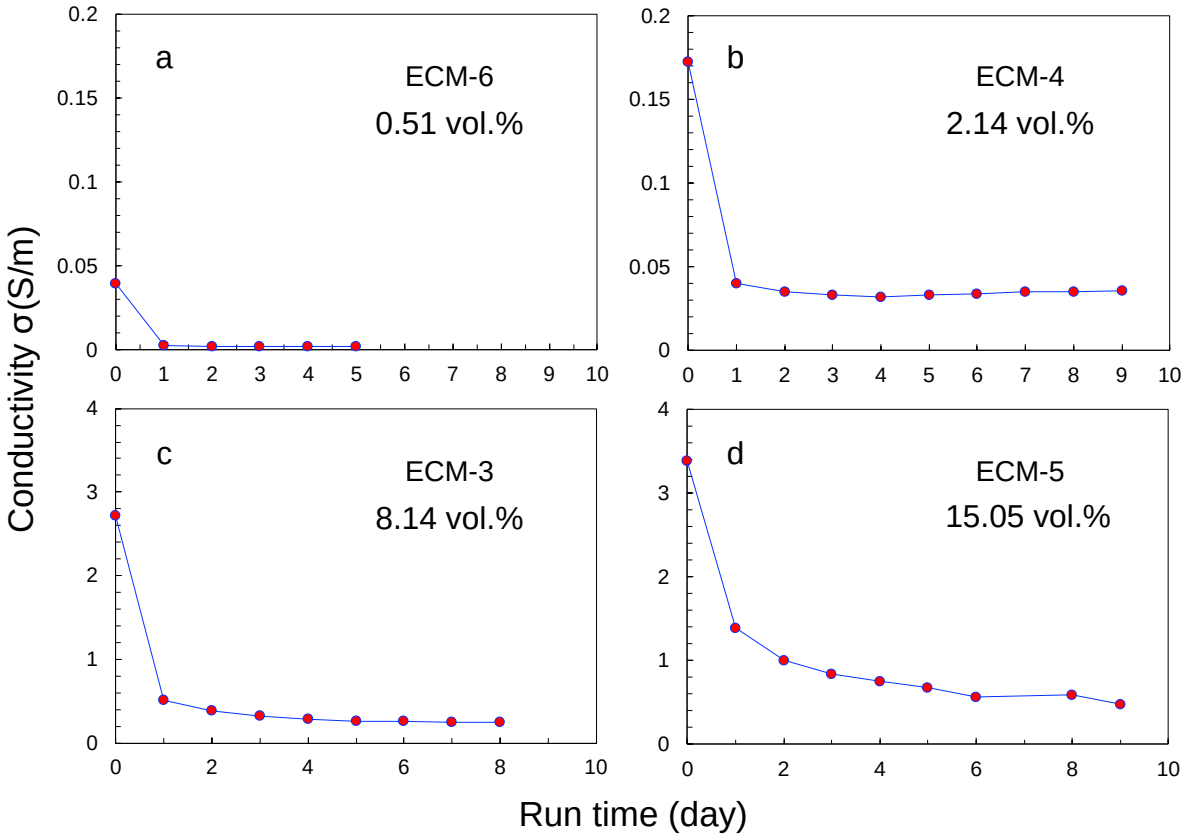

Figure 2. Conductivity variation with run time in the forsterite–H_2O–NaCl system at 800 °C and 1 GPa. The fluid fractions determined in the recovered samples are also shown in each panel. Note that the vertical scale is different for the sub-figures **a, b** and **c, d**.

3.2. Electrical conductivity variation with time

Figure 2 shows the variation in electrical conductivity during each experiment. Experiments were designed to run for 8 days to guarantee textural equilibration, and the electrical conductivity of the samples were measured each day during the run. The experiment with the lowest fluid fraction of 0.51 vol.%, however, was merely run for only 5 days because the thermocouple failed on the fifth day. In all experiments, the conductivity strongly decreased during the first day and then gradually stabilized over time. Most likely, the strong change in conductivity at the beginning of the experiment is related to fluid loss, while the more gradual change after the first day may be related to textural changes.

The conductivity in all systems was essentially stable after 72 h, which indicates that both fluid fraction and fluid geometry remained constant (e.g., Figure 1-d). Therefore, we consider the electrical conductivity measured just before quenching as the electrical conductivity at textural equilibration.

3.3. Electrical conductivity under textural equilibrium conditions

The impedance spectra obtained in the last electrical conductivity measurements of each experiment are shown in Figure 3. For the experiments with fluid fractions of 0.51, 2.14, and 8.14 vol.%, the electrical impedance spectra contain well-developed and complete semi-circle arcs at high frequencies. In these cases, the cell resistance can be obtained from the diameter of the semicircle. For the highest fluid fraction of 15.05 vol.%, the semi-arc disappeared completely and was replaced by a segment under the real axis (Z´), which was most likely caused by inductance of the Pt wires. In this case, the cell resistance was directly obtained from the intercept with the real axis (Z″= 0).

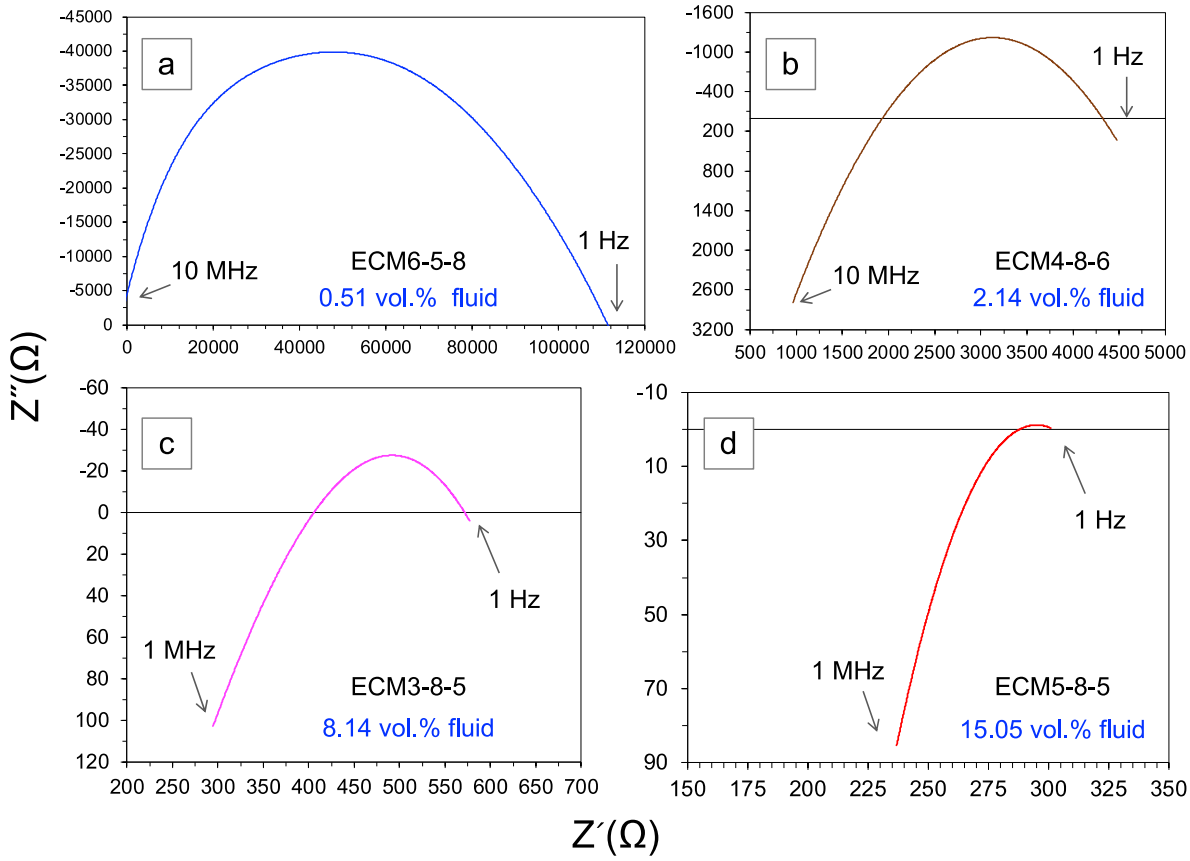
a
10 MHz
ECM6-5-8
0.51 vol.% fluid
1 Hz
b
1 Hz
10 MHz
ECM4-8-6
2.14 vol.% fluid
c
1 Hz
1 MHz
ECM3-8-5
8.14 vol.% fluid
d
1 Hz
1 MHz
ECM5-8-5
15.05 vol.% fluid
Z″(Ω)
Z´(Ω)

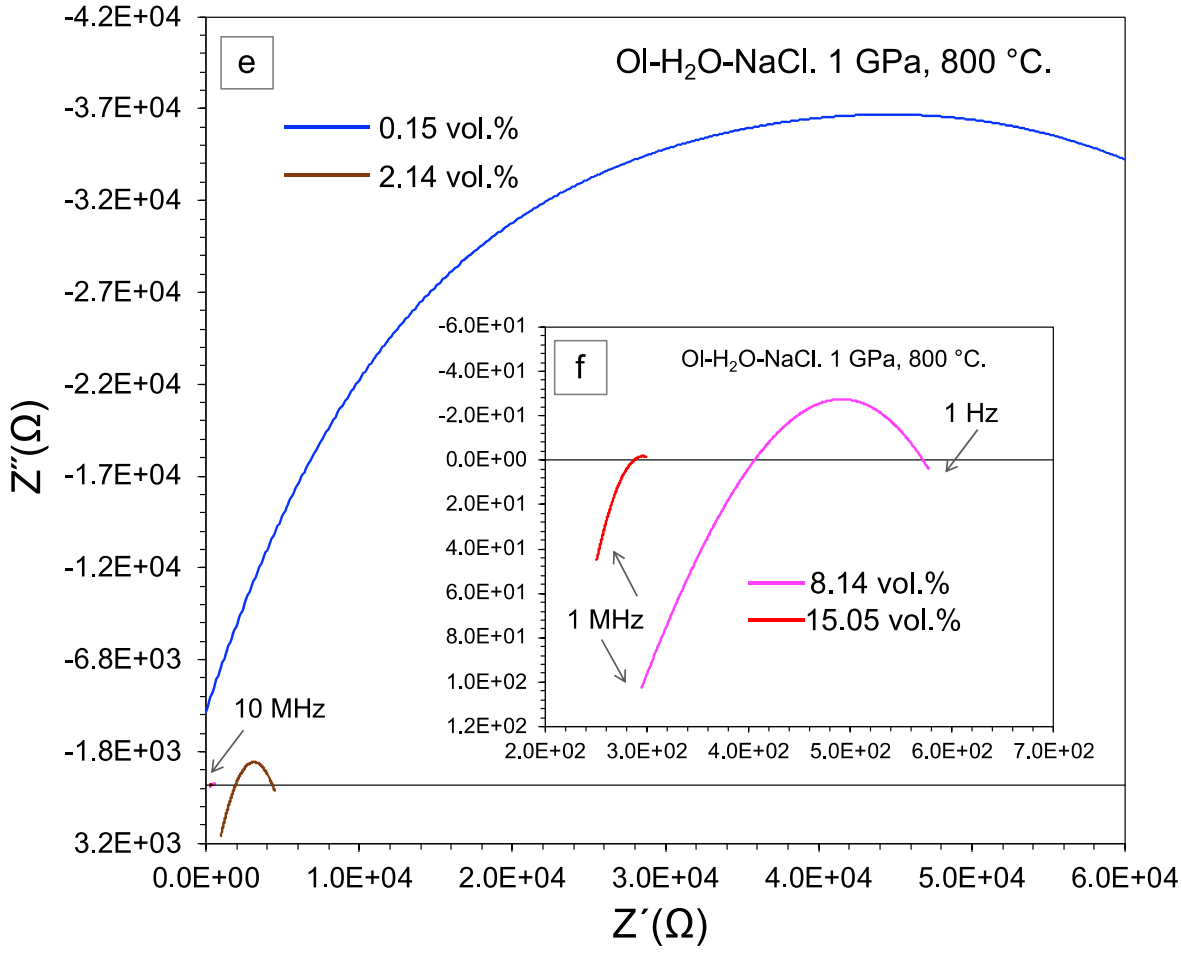
e
Ol-H2O-NaCl. 1 GPa, 800 °C.
0.15 vol.%
2.14 vol.%
10 MHz
f
Ol-H2O-NaCl. 1 GPa, 800 °C.
1 Hz
1 MHz
8.14 vol.%
15.05 vol.%
Z″(Ω)
Z´(Ω)

Figure 3. Impedance spectra of samples with textural equilibrium at different fluid fractions in the forsterite–H_2O–NaCl system at 1 GPa and 800 °C. **(a)** At the lowest fluid fraction of 0.51 vol.%, the sample conductivity is governed by the interior of the forsterite grains, and the resistance may be obtained either from arc fitting or from the intercept with the real axis. **(b and c)** At higher fluid fractions, the sample conductivity is governed mostly by the fluid-bearing grain edges, and the resistance may be obtained either from arc fitting or from the intercept with the real axis. **(d)** At the highest fluid fraction, the resistance may be determined from the Z´ intercept of the spectrum (where $Z''=0$). **(e)** Comparison of the electrical resistances in all investigated fluid fraction systems. The electrical resistance of different fluid fractions shows different magnitudes.

It is expected that the conductivity circuits in forsterite aggregates depend on the geometrical distribution of the present fluid (Roberts & Tyburczy, 1999; Shimojuku et al., 2012). The impedance spectra of the systems in this study are governed by a combination of resistor and capacitor circuits. From a combination of the measured impedance spectra (Figure 3) and visualized 3-D fluid distributions (Figure 4), the conduction circuits in this study can be determined. In low fluid fraction systems with isolated fluid pockets, the sample conductivity is mainly governed by the interior of the forsterite grains, and the electrical circuit is composed of the response of the grain and fluid in a series circuit. In high fluid fraction systems with an interconnected fluid network, the sample conductivity is mostly governed by the fluid tube, and the electrical circuit is composed of the response of the grain interior and fluid-filled grain edges in a parallel circuit.

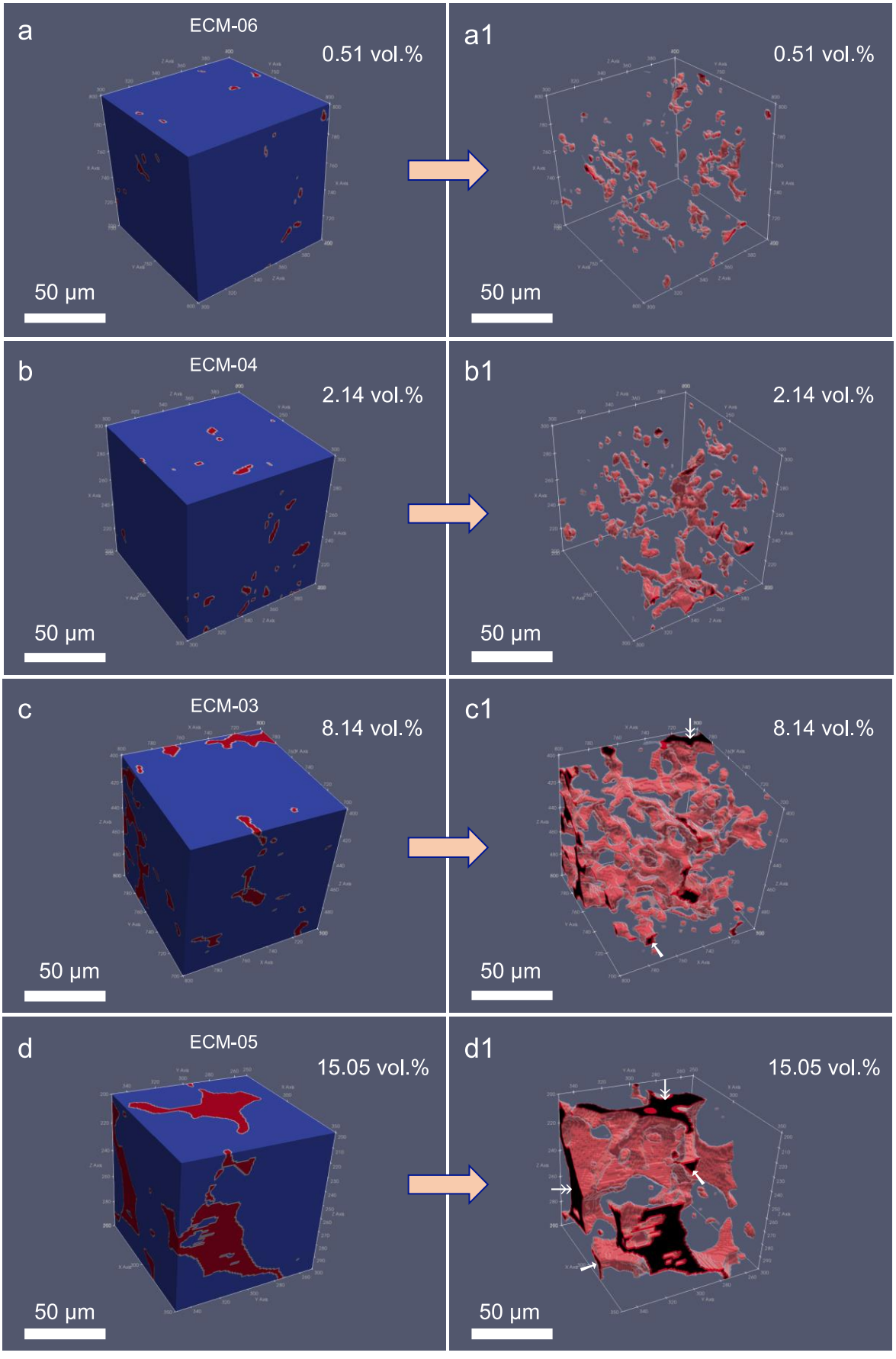
a
ECM-06
0.51 vol.%
50 μm
a1
0.51 vol.%
50 μm
b
ECM-04
2.14 vol.%
50 μm
b1
2.14 vol.%
50 μm
c
ECM-03
8.14 vol.%
50 μm
c1
8.14 vol.%
50 μm
d
ECM-05
15.05 vol.%
50 μm
d1
15.05 vol.%
50 μm
Forsterite
Aqueous fluid
Interior of fluid channel

Figure 4. Three-dimensional (3-D) images of fluid-bearing forsterite aggregates after electrical conductivity measurements. **(a–d)** 3-D images of sub-volumes of recovered samples. **(a1–d1)** 3-D images of the fluid distributions extracted from a–d. Blue areas represent the forsterite aggregates; red areas represent the interfaces between fluids and forsterite crystals; black areas represent the interior of fluid channels. The fluid distribution is relatively localized on smaller scales, and homogenous on larger scales for all samples. The spaces between the fluid are occupied by olivine crystals. The fluid in a1 occurs mostly as isolated fluid pockets. The fluid in b1 is locally interconnected. The fluids in c1 and d1 are well interconnected. In c1 and d1, there is an obvious bottleneck effect, i.e. the interconnected networks are composed of coarse channels (white double-headed arrows) and fine channels (white arrows). The fluid fraction for each sample is also shown. The cube size of all 3-D images is 100 μm × 100 μm ×100 μm.

3.4. 3-D images of fluid distribution

The fluid distribution in the recovered samples was visualized using the software ParaView for the sub-volume 3-D CT images (Figure 4). The fluid distribution is relatively localized on smaller scales, and homogenous on larger scales for all samples. For the system with the lowest fluid fraction of 0.51 vol.%, the aqueous fluid occurred mostly as isolated fluid pockets (Figure 4-a1). In contrast, the aqueous fluid was locally interconnected via tubular pathways in the system with a fluid fraction of 2.14 vol.% (Figure 4-b1). For the higher fluid fractions of 8.14 and 15.05 vol.%, the interstitial fluid was well interconnected (Figure 4-c1, d1), with the diameter of interconnected tubes increasing with increasing fluid fraction.

3.5. Water content in forsterite

The infrared absorption spectra in the range of from 3100 to 3800 cm^{-1} collected on 10 sampling points with the same aperture size of 200 × 200 μm and scanning time of 12 s are shown in Figure 5. The spectra show sharp absorption peaks derived from structurally bound water in forsterite were observed between 3500 and 3750 cm^{-1}. Moreover, a band at 3300 cm^{-1} and a broad absorption background at 3100–3800 cm^{-1} are also visible and most likely represent free water in fluid inclusions in the forsterite crystals and water in some microcracks, grain boundaries, and dislocations of the forsterite aggregate, respectively. The entire absorption range of 3100–3800 cm^{-1} was integrated to calculate the bulk water content of the forsterite aggregate (Figure 5-a, e.g., Ohuchi & Nakamura, 2007). In contrast, to calculate the water content in the forsterite lattice, a linear background was subtracted from the sharp bands at 3500–3750 cm^{-1} (Figure 5-a) and the remaining absorption was integrated, as shown in in Figure 5-b.

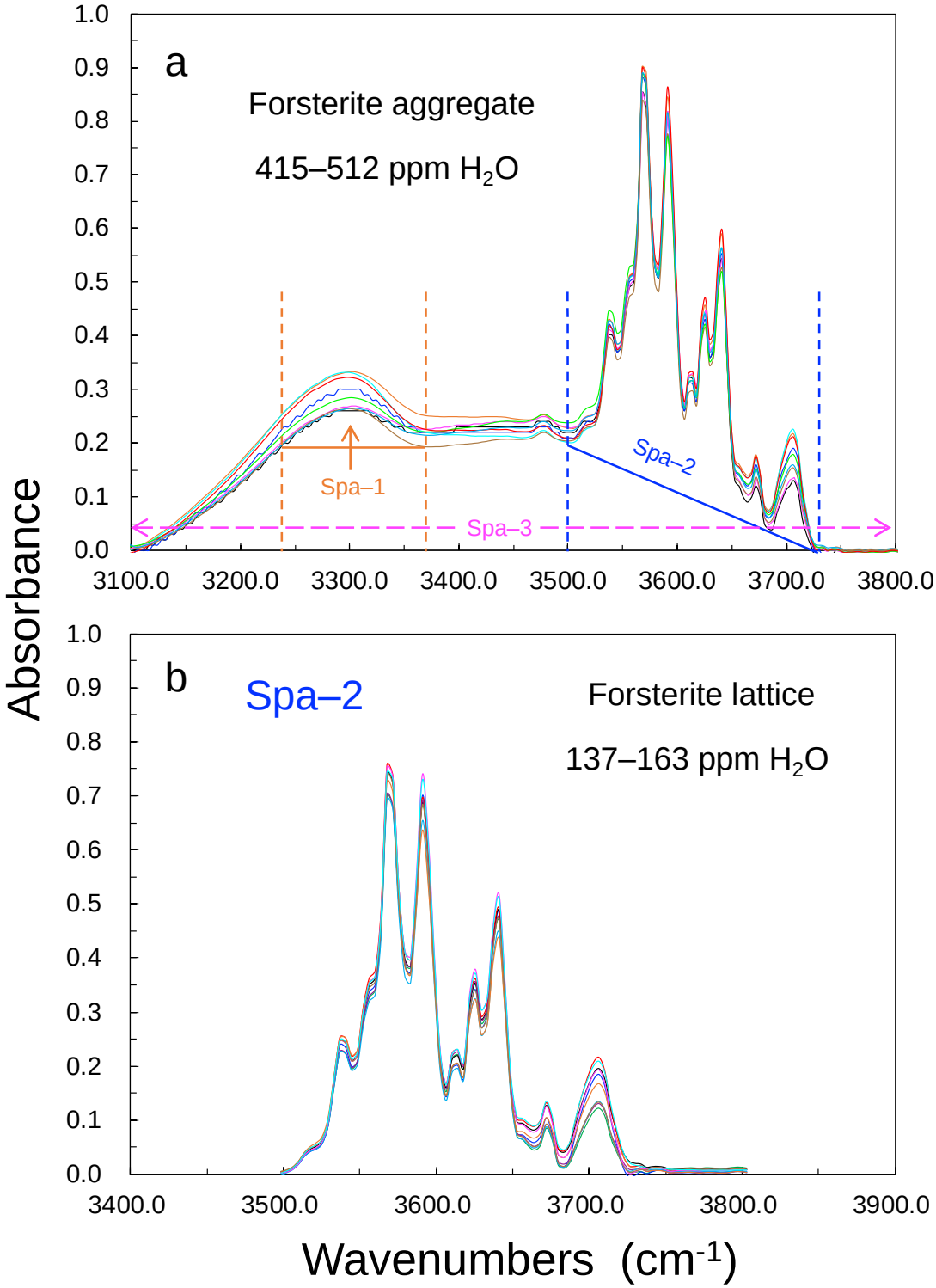

356

357 **Figure 5.** Unpolarized FTIR absorption spectra of the recovered sample ECM-3. The spectra were collected
358 from 10 sampling points with the same aperture size of 200 × 200 μm and scanning time of 12 seconds. The
359 sample thickness is ~300 μm. **(a)** Absorbance spectra in the range of 3100–3800 cm^{-1}. The total area of all
360 absorption peaks between 3100 to 3800 cm^{-1} was integrated to calculate the water content of the forsterite
361 aggregates. The characteristic peaks of the absorption spectra were divided into three types: spa–1, spa–2, and
362 spa–3. Spa–1 at 3300 cm^{-1} is the absorption peak for aqueous fluids in the fluid inclusions of the forsterite

crystals; spa–2 at 3500–3750 cm^{-1} shows the absorption peaks for OH in the forsterite lattice; and spa–3 shows a broad absorption background at 3100–3800 cm^{-1}, which can most likely be attributed to water in some microcracks, grain boundaries, and dislocations, rather than structurally bound water. (b) Absorption spectra between 3500 to 3750 cm^{-1} extracted after baseline correction. The area of these absorption peaks was integrated to calculate the water contents in the forsterite lattice.

To evaluate the effect of the aperture size or scanning time on the bulk water content and forsterite lattice water content, up to 17 infrared absorption spectra were collected in the range of 3100 to 3800 cm^{-1} with various aperture sizes or scanning times. Their respective influence on the water content is shown in Figure S2 and S3 of the Supporting Information. For the 10 sampling points with the same aperture size of 200 × 200 μm and scanning time of 12 s, the bulk water content in the forsterite aggregates ranges from 415 to 512 ppm H_2O with an average of 461 ppm, while the water content in the forsterite lattice ranges from 137 to 163 ppm H_2O with an average of 149 ppm. The bulk water content showed a wider range compared to the water content in the forsterite lattice because of inhomogeneity of the sample.

4. Discussion

4.1. Fluid fraction dependence of electrical conductivity

In Figure 6-a, the electrical conductivities measured in this study are plotted as a function of the fluid fraction as estimated from the CT data. The electrical conductivity steeply increased from 1.65×10^{-3} S/m at 0.51 vol.% to 3.56×10^{-2} S/m at 2.14 vol.%, but increased more slowly with increasing fluid fractions above 2.14 vol.%. At fluid fractions above 8.14 vol.%, the electrical conductivity increased gently. This fluid fraction dependence of the electrical conductivity may reflect the changes in the fluid distribution in the forsterite matrix. The 3-D images showed that the fluid was distributed as isolated pockets at 0.51 vol.% (Figure 4-a1), while it formed an interconnected network at fluid fractions above 2.14 vol.% (Figure 4-b1). This indicates that there is a threshold fluid fraction between 0.51 and 2.14 vol.%. Once the fluid fraction exceeds this critical value, the fluid establishes an interconnected network, shifting the predominant conduction pathway from the forsterite interior to the saline aqueous fluid network. The drastic change in fluid connectivity, therefore, may exert a primary control on the fluid fraction dependence of electrical conductivity. At fluid fractions above 8.14 vol.%, the further increase in conductivity may be related to the enlargement of the average diameter in the fluid network.

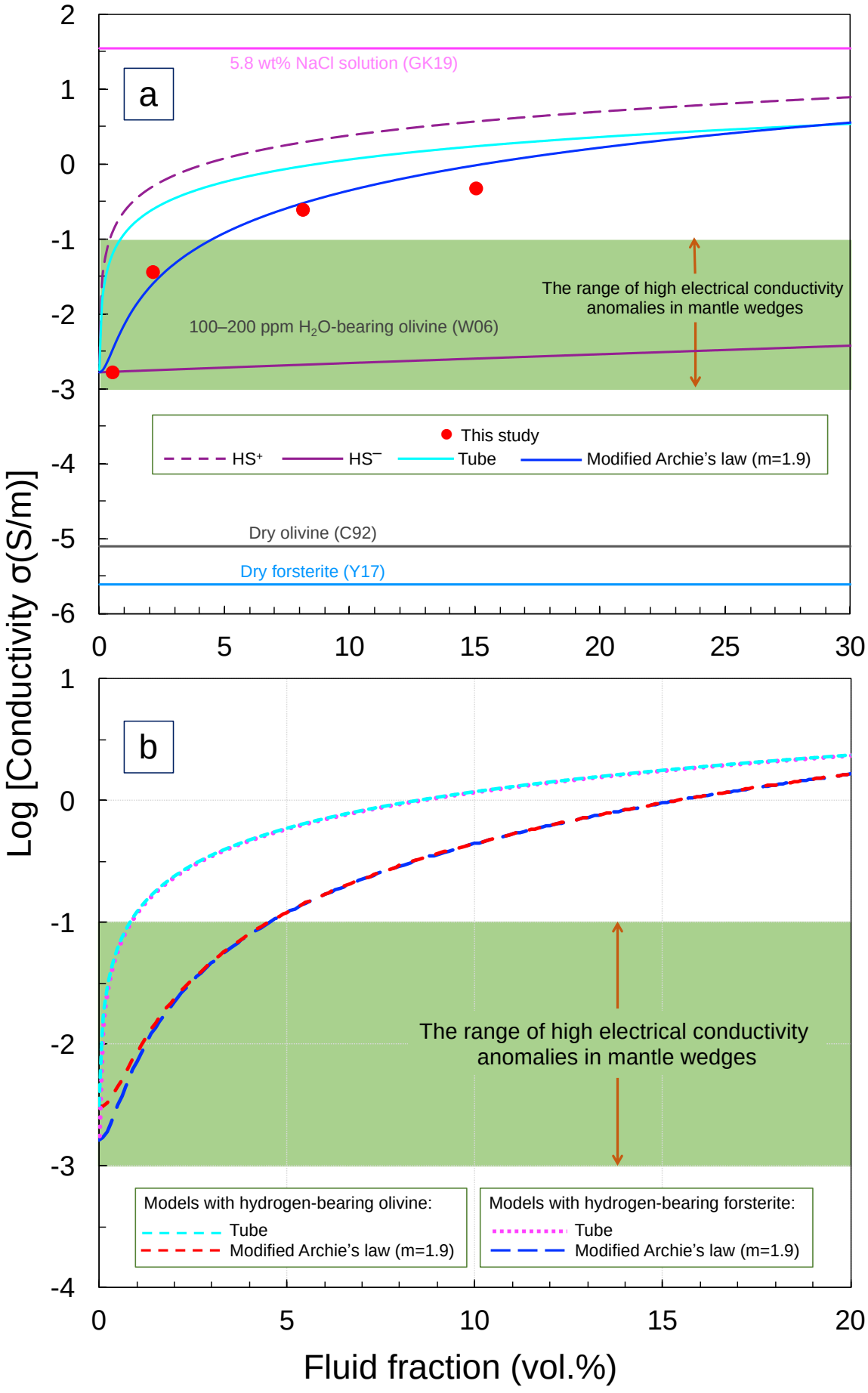
a
5.8 wt% NaCl solution (GK19)
100–200 ppm H_2O-bearing olivine (W06)
The range of high electrical conductivity anomalies in mantle wedges
This study
HS+
HS−
Tube
Modified Archie's law (m=1.9)
Dry olivine (C92)
Dry forsterite (Y17)
b
The range of high electrical conductivity anomalies in mantle wedges
Models with hydrogen-bearing olivine:
Tube
Modified Archie's law (m=1.9)
Models with hydrogen-bearing forsterite:
Tube
Modified Archie's law (m=1.9)
Log [Conductivity σ(S/m)]
Fluid fraction (vol.%)

Figure 6. Fluid fraction dependence of the bulk conductivity. **(a)** Electrical conductivity with textural equilibrium as a function of fluid fraction in the forsterite–H_2O–NaCl system at 800 °C and 1 GPa. The electrical conductivities for single-crystal dry olivine (C92, Constable et al., 1992), dry forsterite aggregate (Y17, Yoshino et al., 2017), 100–200 ppm H_2O-bearing olivine aggregate (W06, Wang et al., 2006), and saline aqueous fluids (GK19, Guo & Keppler, 2019) are shown along with our data. The fluid fraction dependence of several electrical conductivity models (modified Archie's law, Glover et al., 2000; HS upper and lower model, Hashin & Shtrikman, 1962; tube model, Schmeling, 1986) are shown in the diagram. The hydrogen-bearing forsterite conductivity in ECM-6 of this study was used as the solid phase conductivity in all models. **(b)** Effect of iron on the bulk electrical conductivity in the different models. We used the iron-bearing hydrous olivine conductivity (Wang et al., 2006) and hydrogen-bearing forsterite conductivity in ECM-6 of this study for the models. The ranges of the high electrical conductivity anomalies in the mantle wedge are shown as light green areas.

4.2. Charge carriers in the aqueous fluid

Because the conductivity in our study was primarily controlled by the interconnected aqueous fluids, considering the charge carriers in the fluid is important. For the fluids with 5 wt.% NaCl in our study, Na^+ and Cl^- ions produced by dissociation of NaCl are the dominant charge carriers. Manning (2013) reported that the dissociated fraction of NaCl in aqueous fluid at 1 GPa and 800 °C is ~0.82 with a salinity lower than 5.8 wt.%, suggesting that most of the NaCl in the aqueous fluid was dissociated in our experiments. Although their contribution to the bulk electrical conductivity is likely limited, H^+ and OH^- produced by minor H_2O self-dissociation at elevated temperatures and pressures may also play a role as charge carriers (Manning, 2018). Elevated solubility of forsterite in a NaCl-bearing aqueous fluid was observed in previous experimental studies (Macris et al., 2020), suggesting that the solution in our study contained Mg^{2+} and Si^{4+}-bearing species. At a low concentration and nearly neutral pH, the predominant species of dissolved silica is monomeric orthosilicic acid (Manning, 2018), which does not contribute to electrical conduction. Although there may have been several ionic species in the fluid in our samples, the bulk electrical conductivity is most likely controlled by the motion of the dominant Na^+ and Cl^- ions within the interconnected fluid network in a saline aqueous fluid-bearing system (Guo & Keppler, 2019).

4.3. Comparison with the electrical conductivity of fluid-free forsterite aggregates and with pure saline fluids

The bulk electrical conductivities measured in this study in aggregates of forsterite containing saline fluid should fall within the range of inherent conductivities in both end-member systems because no significant charge carriers are released into the aqueous fluid from forsterite grains, as discussed in the Section 4.2. Therefore, to verify the reliability of

our measurements, we compared our results with the electrical conductivities of saline fluid and of fluid-free forsterite aggregates measured in previous studies (Figure 6-a). For saline fluid, the electrical conductivity of aqueous fluid with 5.8 wt.% NaCl measured at 1 GPa and 800 °C was adopted for comparison (Guo & Keppler, 2019). Its reported conductivity is 35 S/m, and significantly higher than the values measured in this study even at the highest fluid fraction of 15.05 vol.%.

Because there is no data of conductivities of hydrous iron-free forsterite aggregates, we compared our data with the conductivity of dry forsterite aggregates at 800 °C and 1 GPa, as calculated with the equation given by Yoshino et al. (2017). Its conductivity of 2.46×10^{-6} S/m is almost three orders of magnitude smaller than the conductivity measured at the lowest fluid fraction of 0.51 vol.% in this study. Water dissolved in forsterite is expected to reduce this difference because it strongly increases the conductivity. The electrical conductivity range of hydrous iron-bearing olivine (X_{Fe} = Fe / (Mg +Fe) = ~0.1) with 100–200 ppm H_2O at 800 °C (Wang et al., 2006, $3.0–4.0 \times 10^{-3}$ S/m) is two to three orders of magnitude higher than that of dry olivine at the same temperature (Constable et al., 1992, 8.0×10^{-6} S/m). Therefore, the conductivity of hydrous forsterite aggregates with 137–163 ppm H_2O, as in this study, may be comparable to or slightly smaller than that of the fluid-bearing hydrous forsterite aggregates at the lowest fluid fraction of 0.51 vol.%. These comparisons show that the conductivities measured in this study are between those in fluid-free forsterite aggregates and those in saline fluids reported in previous studies, demonstrating the reliability of our measurements.

4.4. Comparison with models of electrical conductivity in the fluid-bearing rocks

In this section, we compare the electrical conductivities measured in this study to those predicted using models with simple fluid geometries. The HS upper and lower bound model (Hashin & Shtrikman, 1962), the cube model (Waff, 1974), the tube model (Schmeling, 1986), and a modified Archie's law (Glover et al., 2000) have been proposed to describe the effect of the fluid fraction on bulk electrical conductivity.

The HS model (Hashin & Shtrikman, 1962) provides the upper (HS^+) and lower bounds (HS^-) on the bulk conductivities of fluid–rock mixtures assuming extreme cases of fluid geometry, i.e., completely interconnected fluid films along grain boundaries (dihedral

angle = 0°) or isolated fluid pockets (dihedral angle > 60°). The two extremes are described by the following equations:

$$HS^{+}: \sigma_b = \sigma_f \left(1 - \frac{3(1-\phi)(\sigma_f - \sigma_s)}{3\sigma_f - \phi(\sigma_f - \sigma_s)}\right), \quad (2)$$

$$HS^{-}: \sigma_b = \sigma_s \left(1 + \frac{3\phi(\sigma_f - \sigma_s)}{3\sigma_s + (1-\phi)(\sigma_f - \sigma_s)}\right), \quad (3)$$

where σ_f, σ_s, and ϕ are the electrical conductivity of the fluid, the solid matrix, and the fluid fraction, respectively. The cube model (Waff, 1974) assumes that cubic grains with low conductivity and uniform grain size are surrounded by a high-conductivity fluid layer of uniform thickness. The result of this model is similar to that of the HS^{+} model. Its approximate bulk conductivity is described as follows:

$$\sigma_b = \frac{2}{3}\sigma_f \phi + \sigma_s (1-\phi). \quad (4)$$

In the tube model (Schmeling, 1986), the fluid is assumed to be distributed as a rectangular tube network along the grain edges, but with unwetted grain boundaries:

$$\sigma_b = \frac{1}{3}\sigma_f \phi + \sigma_s (1-\phi)\,. \quad (5)$$

Based on the above equations, it is obvious that the tube model gives a lower conductivity than the cube model.

Archie's law is an empirical relation between the fluid fraction and bulk conductivity (Archie, 1942), which is commonly applied to describe the electrical conductivity of a porous sandstone. The conventional Archie's law is designed for a conductive phase saturating a non-conductive matrix at shallow depths and low temperatures, where the conductivity of the matrix is negligible, whereas the conductivities of rock-forming minerals at high P–T conditions may significantly contribute to the bulk conductivity (Glover et al., 2000). To include the effect of solid conductivity, a modified form of the conventional Archie's law (modified Archie's law) was proposed by Glover et al., (2000) as follows:

$$\sigma_b = \sigma_f \phi^m + \sigma_s (1-\phi)^p, \quad (7)$$

$$p = \frac{\log(1-\phi^m)}{\log(1-\phi)}, \quad (8)$$

where the exponents m and p represent the connectivity of the fluid and solid phases, respectively. This model allows a change in fluid connectivity according to the fluid fraction.

In Figure 6-a, our results are compared with those of the models. For the model calculations, we assumed σ_f = 35 S/m for the conductivity of aqueous fluid with a salinity of 5.8 wt.% (Guo & Keppler, 2019). For σ_s, we used the conductivity of the system with the lowest fluid fraction in this study (i.e., σ_s = 1.65 × 10^{-3} S/m) in which the fluid was not interconnected as revealed by 3-D images (Figure 4-a1); thus, the effect of fluid on the conductivity could be minor. Our conductivities fall within the range of those of the HS models and thus do not violate the physical bounds. Because the dihedral angle defined by the curved olivine-fluid interfaces is smaller than 60° in the olivine + saline fluid system at 800 °C and 1 GPa with a NaCl concentration of 5.0 wt.% (Huang et al., 2019), the fluid in our experiments is expected to be distributed along the triple junctions and result in mostly the same conductivities as in the tube model. However, our conductivities are actually smaller than those of the tube model (Figure 6-a). There are two plausible reasons for this discrepancy. First, this discrepancy may be attributed to the interfacial anisotropy of forsterite in our system, which would lead to a range of true dihedral angles having the different wetting properties in different crystallographic orientations. Along with the curved forsterite-fluid interfaces, for example, faceted planes were observed in all the recovered samples (Figure 1). At low fluid fractions, the fluid pores surrounded by faceted planes have difficulty forming an interconnected network even at dihedral angles smaller than 60° (Price et al., 2006), while they can be interconnected at relatively high fluid fractions depending on the dihedral angle. This could result in the establishment of fluid interconnections at a range of fluid fractions, which is consistent with the change in fluid connectivity according to the fluid fractions confirmed by our CT images. Second, the normal grain growth driven by Ostwald ripening results in a heterogeneous grain size distribution ranging from 5 to 100 μm in our systems (Figure 1), which plays a significant role for the fluid distribution and thus the permeability (e.g., Cerpa et al., 2017; Wark & Watson, 2000). The fluid is expected to be concentrated in domains with finer grain sizes, assuming the presence of curved interfacial boundaries everywhere in a fluid-bearing, deep-seated rock system. Although the presence of faceted interfacial boundaries may decrease the degree of fluid redistribution, the

permeability in domains with finer grain sizes will match or exceed that in domains with coarser grain sizes (Wark & Watson, 2000). However, this fluid localization induced by the above two factors, to some extent increases the tortuosity of the fluid path on the whole rock scale, which might hamper the enhancement of the bulk electrical conductivity and lead to a deviation of the bulk electrical conductivity obtained in the present study from an idealized tube model. As revealed by the CT images, a certain volume fraction of fluid is required to establish the interconnected networks in the fluid-bearing forsterite aggregates. Furthermore, even for the high fluid fraction systems, in which the fluid was well interconnected, our conductivities were still smaller than those of the tube model. One plausible explanation for this is the variation in tube diameter along the tubes as modeled by Watanabe and Peach (2002), which is consistent with the bottleneck effect observed in the 3-D images of this study.

Although the modified Archie's law is derived from the empirical Archie's law, it considers both the conductivities of solid and fluid phases and describes the change in the degree of fluid connectivity with increasing fluid fraction, which could be an appropriate mixing model for determining the fluid fraction dependence of our conductivities, as discussed in the Section 4.1. Therefore, we used the modified Archie's law to fit our data with a variable cementation exponent (m), and found that the m value of 1.9 best explains our data (Figure 6-a).

5. Implication: Estimation of fluid fractions in fore-arc mantle wedges

An increasing number of MT studies have found the presence of high electrical conductivity anomalies (0.001–1 S/m) in the deep fore-arc regions of Cascadia (Jiracek et al., 1989; Soyer & Unsworth, 2006; Wannamaker et al., 2014), Mexico (Jödicke et al., 2006), Costa Rica (Worzewski et al., 2011), North Chile (Araya Vargas et al., 2019; Brasse, 2002; Schwalenberg et al., 2002), North Honshu (Mishina, 2009), Southern Kyushu (Ichiki et al., 2000), Ryukyu–Philippine (Shimakawa & Honkura, 1991), and New Zealand (Wannamaker et al., 2002 and 2009). These high electrical conductivity anomalies are most likely due to the presence of slab-derived aqueous fluids. In hot subduction zones such as Cascadia and Mexico, fluids liberated from the shallow subducting slabs at depths of 30–60 km can penetrate through the highly serpentinized mantle wedge and accumulate in the deep fore-arc region (Nakatani & Nakamura, 2016; Reynard et al., 2011). In intermediate and cold subduction zones, in contrast, saline fluid liberated at a depth of ~80 km can penetrate all the

542 way through the fore-arc mantle wedge without mantle melting and serpentinization due to
543 low dihedral angles (Huang et al., 2019). Therefore, our experimental results can be applied
544 to MT data of intermediate and cold subduction zones where the slab-derived saline fluids
545 can be present in the non-serpentinized fore-arc mantle. Remarkably high electrical
546 conductivity anomalies of 0.1–1 S/m were often observed in crustal regions where the
547 dominant minerals are not olivine. We thus focus on the high electrical conductivity
548 anomalies of 0.001–0.1 S/m detected at mantle depths.

549 Our experimental results provide a realistic relationship between the electrical
550 conductivity and fluid fractions in the forsterite-saline fluid system at 800 °C and 1 GPa, with
551 a fluid with a NaCl concentration of 5 wt.%, under conditions of textural equilibrium. In
552 natural mantle settings, however, olivine contains iron, which enhances the electrical
553 conductivity of the olivine matrix through polaron conduction (Fei et al., 2020; Yoshino &
554 Katsura, 2013). To incorporate the effect of iron into the conductivity–fluid fraction
555 relationship, we recalculated the bulk conductivity by using the conductivity of hydrous iron-
556 bearing olivine aggregate (3.0×10^{-3} S/m, Wang et al., 2006) according to the modified
557 Archie's law with m =1.9 and the tube model (Figure 6-b). The results showed that the
558 difference in the bulk conductivity is negligible between the iron-free and iron-bearing
559 systems when the fluid forms an interconnected network in the models (i.e., the modified
560 Archie's law at fluid fractions above ~1 vol.% and the tube model). At fluid fractions below
561 1 vol.%, the bulk conductivity of the modified Archie's law is slightly higher in the iron-
562 bearing system than in the iron-free system due to the contribution of the matrix conductivity.

563 In Figure 6-b, the range of electrical conductivity anomalies (0.001–0.1 S/m) detected
564 in fore-arc mantle wedges is shown. Based on the modified Archie's law calibrated by our
565 experimental data, the presence of ~1.0–5.0 vol.% aqueous fluid with 5.0 wt.% NaCl is
566 required to cause the high electrical conductivity anomalies of 0.01–0.1 S/m in fore-arc
567 mantle wedges. This result does not depend on the iron concentration of olivine, and is
568 almost consistent with a fluid fraction of ~ 2.0 vol.% for most mantle wedges (Iwamori,
569 1998). The anomalies of 0.003–0.01 S/m may represent less interconnected fluid pores with
570 fluid fractions below 1.0 vol.% in the iron-bearing olivine matrix. The lower conductivities of
571 0.001–0.003 S/m may be attributed to iron-bearing olivine with a water content smaller than
572 100–200 ppm under fluid-unsaturated conditions. The conventional tube model would lead to
573 lower fluid fractions of ~0–0.8 vol.% for the anomalies of 0.003–0.1 S/m. The large

difference in the estimated fluid fractions between our model (i.e., ~1.0–5.0 vol.%) and the conventional tube model (i.e., ~0–0.8 vol.%) emphasizes the importance of our experimental data, which describe the realistic fluid distribution with interfacial anisotropy at mantle conditions.

The effects of temperature, pressure, and fluid compositions on the estimated electrical conductivity should be considered. Salinity significantly affects the conductivity because salt acts as an effective charge carrier in the form of dissociated ions (Guo & Keppler, 2019) and also increases the solubility of olivine, which increases the solute concentration in the fluids and affects the fluid geometry by changing the dihedral angle (Huang et al, 2019). The original salinity of the slab-derived fluid produced by dehydration reactions has been estimated to be 0.5–2.0 wt.% (Li & Hermann, 2015), but it can be enhanced during the fluid ascent in the fore-arc mantle wedge owing the preferential incorporation of water into the mantle minerals (Bernini et al., 2013; Reynard, 2016; Reynard et al., 2011). The salinity of 5.0 wt.% used in this study is plausible because comparable values were reported in upwelling slab-derived fluids (6.6 wt.%, Kusuda et al., 2014; Matsubaya et al., 1973) and fluid inclusions in a mantle xenolith (4.1–6.1 wt.%, Kawamoto et al., 2013). In addition, it does not deviate much from the salinity of seawater (3.5 wt.%), which is likely representative of pore fluids expelled by mechanical compaction in the shallow part of subduction zones. Carbon dioxide in the fluid may decrease the olivine-fluid dihedral angles at low-T and high-P conditions corresponding to fore-arc mantle wedges (Huang et al., 2020). The higher P–T conditions expected at greater depths enhance the conductivity of the fluid (Guo & Keppler, 2019) and the olivine solubility (Yoshino et al., 2007). The presence of pyroxenes may also increase the solubility of olivine (Tiraboschi et al., 2018) and decrease the olivine-fluid dihedral angle (Huang et al., 2020). These factors more or less increase the bulk conductivity to some extent, thereby lowering the estimated fluid fractions, although further experimental constraints are needed. Therefore, our data could provide the upper bound on the estimated fluid fraction in the fore-arc mantle. Nevertheless, the presence of significant amounts of aqueous fluid in the mantle suggests intense fluid circulation through the fore-arc mantle wedge in subduction zones.

6. Conclusion

In this study, we measured the electrical conductivity of fluid-bearing forsterite aggregates with various fluid fractions and a constant salinity of 5.0 wt.% NaCl in the fluid at

1 GPa and 800 °C. Textural equilibrium was achieved owing to the long run durations of up to 8 days applied in this study. This was verified by the concentrated grain size distribution with a peak close to the mean grain size and the attainment of balance of interfacial tension at triple junctions. Our results enable us to establish a more realistic relationship between fluid fraction and bulk electrical conductivity in a non-ideal system, and to precisely estimate the fluid fraction in mantle wedges.

We found that the electrical conductivity increases nonlinearly with increasing fluid fractions, and that the modified Archie's law reproduces the experimental data very well. The 3-D microstructure of the interstitial pores determined by synchrotron X-ray CT shows a change in fluid distribution from isolated pockets to interconnected networks with increasing fluid fraction, accounting for the nonlinear increase in the electrical conductivity. Although the dihedral angle in the olivine-fluid system with a salinity of 5 wt.% is smaller than the critical value of 60° at 1 GPa and 800 °C (Huang et al, 2019), the interfacial anisotropy of forsterite and the difference in grain size might localize the fluid distribution and further hamper the bulk electrical conductivity. These factors result in a deviation of the electrical conductivity obtained in our study from the idealized tube model. Moreover, a rapid increase in bulk conductivity indicates that a threshold fluid fraction exists between 0.51 and 2.14 vol.%, beyond which interconnected fluid networks form, which is consistent with the visualized 3-D fluid distributions in the recovered samples. Our results provide direct evidence that the presence of > 1.0 vol.% aqueous fluid with moderate salinity is required to explain the high conductivity anomalies above 0.01 S/m detected in fore-arc mantle wedges.

Acknowledgments

We are grateful to Catherine McCammon for her technical support in the piston cylinder experiments. We would like to thank Wakana Fujita for providing directions for the CT imaging process. This work was supported by JSPS KAKENHI Grant Nos. JP16H06348 and JP16K13903 awarded to M. Nakamura, JSPS Japanese–German Graduate Externship, International Joint Graduate Program in Earth and Environmental Sciences, Tohoku University (GP-EES), and by the Ministry of Education, Culture, Sports, Science and Technology (MEXT) of Japan under its Earthquake and Volcano Hazards Observation and Research Program, and by the Core Research Cluster of Disaster Science in Tohoku University (Designated National University). The synchrotron radiation experiments were performed at SPring-8 with the approval of the Japan Synchrotron Radiation Research

Institute (JASRI) (proposal nos. 2018A1471, 2018A1464, 2019B1785). We provide the datasets on figshare (https://doi.org/10.6084/m9.figshare.13245194.v1), including the electrical conductivity measurement, 3-D CT image, grain size distribution, and FTIR data, to support our research.

Reference

Araya Vargas, J., Meqbel, N. M., Ritter, O., Brasse, H., Weckmann, U., Yáñez, G., & Godoy, B. (2019). Fluid Distribution in the Central Andes Subduction Zone Imaged With Magnetotellurics. *Journal of Geophysical Research: Solid Earth*, *124*(4), 4017–4034. https://doi.org/10.1029/2018JB016933

Archie, G. E. (1942). The electrical resistivity log as an aid in determining some reservoir characteristics. *Transactions of the AIME*, *146*(01), 54-62. https://doi.org/10.2118/942054-G

Bell, D. R., Rossman, G. R., Maldener, J., Endisch, D., & Rauch, F. (2003). Hydroxide in olivine: A quantitative determination of the absolute amount and calibration of the IR spectrum. *Journal of Geophysical Research: Solid Earth*, *108*(B2). https://doi.org/10.1029/2001jb000679

Bernini, D., Wiedenbeck, M., Dolejš, D., & Keppler, H. (2013). Partitioning of halogens between mantle minerals and aqueous fluids: Implications for the fluid flow regime in subduction zones. *Contributions to Mineralogy and Petrology*, *165*(1), 117–128. https://doi.org/10.1007/s00410-012-0799-4

Bloch, W., John, T., Kummerow, J., Salazar, P., Krüger, O. S., & Shapiro, S. A. (2018). Watching Dehydration: Seismic Indication for Transient Fluid Pathways in the Oceanic Mantle of the Subducting Nazca Slab. *Geochemistry, Geophysics, Geosystems*, *19*(9), 3189–3207. https://doi.org/10.1029/2018GC007703

Brasse, H. (2002). The Bolivian Altiplano conductivity anomaly. *Journal of Geophysical Research*, *107*(B5). https://doi.org/10.1029/2001jb000391

Cerpa, N. G., Wada, I., & Wilson, C. R. (2017). Fluid migration in the mantle wedge: Influence of mineral grain size and mantle compaction. *Journal of Geophysical Research: Solid Earth*, *122*(8), 6247–6268. https://doi.org/10.1002/2017JB014046

Constable, S., Shankland, T. J., & Duba, A. (1992). The electrical conductivity of an isotropic olivine mantle. *Journal of Geophysical Research*, *97*(B3), 3397–3404. https://doi.org/10.1029/91JB02453

Dai, L. (2009). Electrical conductivity of orthopyroxene: Implications for the water content of the asthenosphere. *Proc. Jpn. Acad., Ser. B*, *85*. https://doi.org/10.2183/pjab.85.466

Ducea, M. N., & Park, S. K. (2000). Enhanced Mantle Conductivity from Sulfide Minerals, Southern Sierra Nevada, California. *Geophysical Research Letters*, *27*(16), 2405–2408. https://doi.org/10.1029/2000GL011565

Faul, U. H. (1997). Permeability of partially molten upper mantle rocks from experiments and percolation theory. *Journal of Geophysical Research: Solid Earth*, *102*(B5), 10299–10311. https://doi.org/10.1029/96jb03460

Fei, H., Druzhbin, D., & Katsura, T. (2020). The Effect of Water on Ionic Conductivity in Olivine. *Journal of Geophysical Research: Solid Earth*, *125*(3). https://doi.org/10.1029/2019JB019313

Frost, B. R., Fyfe, W. S., Tazaki, K., & Chan, T. (1989). Grain-boundary graphite in rocks and implications for high electrical conductivity in the lower crust. *Nature*, *340*(6229), 134–136. https://doi.org/10.1038/340134a0

Glover, P. W.J. (1996). Graphite and electrical conductivity in the lower continental crust: A review. *Physics and Chemistry of the Earth*. https://doi.org/10.1016/S0079-1946(97)00049-9

Glover, Paul W.J., Hole, M. J., & Pous, J. (2000). A modified Archie's law for two conducting phases. *Earth and Planetary Science Letters*, *180*(3–4), 369–383. https://doi.org/10.1016/S0012-821X(00)00168-0

Guo, H., & Keppler, H. (2019). Electrical Conductivity of NaCl-Bearing Aqueous Fluids to 900 °C and 5 GPa. *Journal of Geophysical Research: Solid Earth*, *124*(2), 1397–1411.

https://doi.org/10.1029/2018JB016658
Guo, X., Yoshino, T., & Shimojuku, A. (2015). Electrical conductivity of albite-(quartz)-water and albite-water-NaCl systems and its implication to the high conductivity anomalies in the continental crust. *Earth and Planetary Science Letters*, *412*, 1–9. https://doi.org/10.1016/j.epsl.2014.12.021
Hashin, Z., & Shtrikman, S. (1962). A Variational approach to the theory of the effective magnetic permeability of multiphase materials. *Journal of Applied Physics*, *33*(10), 3125–3131. https://doi.org/10.1063/1.1728579
Hermann, J., Spandler, C., Hack, A., & Korsakov, A. V. (2006). Aqueous fluids and hydrous melts in high-pressure and ultra-high pressure rocks: Implications for element transfer in subduction zones. *Lithos*, *92*(3–4), 399–417. https://doi.org/10.1016/j.lithos.2006.03.055
Holness, M. B. (1992). Equilibrium dihedral angles in the system quartz–CO_2–H_2O–NaCl at 800 °C and 1–15 kbar: the effects of pressure and fluid composition on the permeability of quartzites. *Earth and Planetary Science Letters*, *114*(1), 171–184. https://doi.org/10.1016/0012-821X(92)90159-S
Holness, M. B. (1993). Temperature and pressure dependence of quartz-aqueous fluid dihedral angles: the control of adsorbed H_2O on the permeability of quartzites. *Earth and Planetary Science Letters*, *117*(3–4), 363–377. https://doi.org/10.1016/0012-821X(93)90090-V
Huang, Y., Nakatani, T., Nakamura, M., & McCammon, C. (2019). Saline aqueous fluid circulation in mantle wedge inferred from olivine wetting properties. *Nature Communications*, *10*(1), 5557. https://doi.org/10.1038/s41467-019-13513-7
Huang, Y., Nakatani, T., Nakamura, M., & McCammon, C. (2020). Experimental constraint on grain-scale fluid connectivity in subduction zones. *Earth and Planetary Science Letters*, *552*, 116610. https://doi.org/10.1016/j.epsl.2020.116610
Ichiki, M., Sumitomo, N., & Kagiyama, T. (2000). Resistivity structure of high-angle subduction zone in the southern Kyushu district, southwestern Japan. *Earth, Planets and Space*, *52*(8), 539–548. https://doi.org/10.1186/BF03351661
Iwamori, H. (1998). Transportation of H_2O and melting in subduction zones. *Earth and Planetary Science Letters*, *160*(1–2), 65–80. https://doi.org/10.1016/S0012-821X(98)00080-6
Jiracek, G. R., Curtis, J. H., Ramirez, J., Martinez, M., & Romo, J. (1989). Two-dimensional magnetotelluric inversion of the EMSLAB Lincoln Line. *Journal of Geophysical Research*, *94*(B10). https://doi.org/10.1029/jb094ib10p14145
Jödicke, H., Jording, A., Ferrari, L., Arzate, J., Mezger, K., & Rüpke, L. (2006). Fluid release from the subducted Cocos plate and partial melting of the crust deduced from magnetotelluric studies in southern Mexico: Implications for the generation of volcanism and subduction dynamics. *Journal of Geophysical Research*, *111*(B8), B08102. https://doi.org/10.1029/2005JB003739
Kawamoto, T., Yoshikawa, M., Kumagai, Y., Mirabueno, M. H. T., Okuno, M., & Kobayashi, T. (2013). Mantle wedge infiltrated with saline fluids from dehydration and decarbonation of subducting slab. *Proceedings of the National Academy of Sciences of the United States of America*, *110*(24), 9663–9668. https://doi.org/10.1073/pnas.1302040110
Kusuda, C., Iwamori, H., Nakamura, H., Kazahaya, K., & Morikawa, N. (2014). Arima hot spring waters as a deep-seated brine from subducting slab. *Earth, Planets and Space*, *66*(1). https://doi.org/10.1186/1880-5981-66-119
Li, H., & Hermann, J. (2015). Apatite as an indicator of fluid salinity: An experimental study of chlorine and fluorine partitioning in subducted sediments. *Geochimica et Cosmochimica Acta*, *166*, 267–297. https://doi.org/10.1016/j.gca.2015.06.029
Liu, X., Matsukage, K. N., Li, Y., Takahashi, E., Suzuki, T., & Xiong, X. (2018). Aqueous Fluid Connectivity in Subducting Oceanic Crust at the Mantle Transition Zone Conditions. *Journal of Geophysical Research: Solid Earth*. https://doi.org/10.1029/2018JB015973
Macris, C. A., Newton, R. C., Wykes, J., Pan, R., & Manning, C. E. (2020). Diopside, enstatite and forsterite solubilities in H_2O and H_2O–NaCl solutions at lower crustal and upper mantle conditions. *Geochimica et Cosmochimica Acta*, *279*, 119–142. https://doi.org/10.1016/j.gca.2020.03.035
Manning, C. E. (2013). Thermodynamic modeling of fluid-rock interaction at mid-crustal to upper-mantle conditions. *Reviews in Mineralogy and Geochemistry*, *76*(1), 135-164.

https://doi.org/10.2138/rmg.2013.76.5
Manning, C. E. (2018). Fluids of the Lower Crust: Deep Is Different. *Annual Review of Earth and Planetary Sciences*, *46*(1), 67–97. https://doi.org/10.1146/annurev-earth-060614-105224
Manthilake, G., Bolfan-Casanova, N., Novella, D., Mookherjee, M., & Andrault, D. (2016). Dehydration of chlorite explains anomalously high electrical conductivity in the mantle wedges. *Science Advances*, *2*(5), e1501631. https://doi.org/10.1126/sciadv.1501631
Matsubaya, O., Sakai, H., Kusachi, I., & Satake, H. (1973). Hydrogen and oxygen isotopic ratios and major element chemistry of Japanese thermal water systems. *Geochemical Journal*, *7*(3), 123–151. https://doi.org/10.2343/geochemj.7.123
Mishina, M. (2009). Distribution of crustal fluids in Northeast Japan as inferred from resistivity surveys. *Gondwana Research*, *16*(3–4), 563–571. https://doi.org/10.1016/j.gr.2009.02.005
Nakatani, T., & Nakamura, M. (2016). Experimental constraints on the serpentinization rate of fore-arc peridotites: Implications for the upwelling condition of the slab-derived fluid. *Geochemistry, Geophysics, Geosystems*, *17*(8), 3393–3419. https://doi.org/10.1002/2016GC006295
Ni, H., Keppler, H., & Behrens, H. (2011). Electrical conductivity of hydrous basaltic melts: Implications for partial melting in the upper mantle. *Contributions to Mineralogy and Petrology*, *162*(3), 637–650. https://doi.org/10.1007/s00410-011-0617-4
Ohuchi, T., & Nakamura, M. (2006). Microstructure evolution of aqueous fluid-bearing wehrlites: Implications for the fluid distribution in polymineralic rocks. *Journal of Geophysical Research*, *111*(B1), B01201. https://doi.org/10.1029/2004JB003340
Ohuchi, T., & Nakamura, M. (2007). Grain growth in the forsterite-diopside system. *Physics of the Earth and Planetary Interiors*, *160*(1), 1–21. https://doi.org/10.1016/j.pepi.2006.08.003
Pommier, A., GAillArd, F., Malki, M., & PichAvAnt, M. (2010). Methodological re-evaluation of the electrical conductivity of silicate melts. *American Mineralogist*, *95*(2–3), 284–291. https://doi.org/10.2138/am.2010.3314
Pommier, Anne, & Evans, R. L. (2017). Constraints on fluids in subduction zones from electromagnetic data. *Geosphere*, *13*(4), 1026–1049. https://doi.org/10.1130/GES01473.1
Price, J. D., Wark, D. A., Watson, E. B., & Smith, A. M. (2006). Grain-scale permeabilities of faceted polycrystalline aggregates. *Geofluids*, *6*(4), 302–318. https://doi.org/10.1111/j.1468-8123.2006.00149.x
Reynard, B. (2016). Mantle hydration and Cl-rich fluids in the subduction forearc. *Progress in Earth and Planetary Science*. Springer Berlin Heidelberg. https://doi.org/10.1186/s40645-016-0090-9
Reynard, B., Mibe, K., & de Moortèle, B. Van. (2011). Electrical conductivity of the serpentinised mantle and fluid flow in subduction zones. *Earth and Planetary Science Letters*, *307*(3–4), 387–394. https://doi.org/10.1016/J.EPSL.2011.05.013
Rippe, D., Unsworth, M. J., & Currie, C. A. (2013). Magnetotelluric constraints on the fluid content in the upper mantle beneath the southern Canadian Cordillera: Implications for rheology. *Journal of Geophysical Research: Solid Earth*, *118*(10), 5601–5624. https://doi.org/10.1002/jgrb.50255
Roberts, J. J., & Tyburczy, J. A. (1999). Partial-melt electrical conductivity: Influence of melt composition. *Journal of Geophysical Research: Solid Earth*, *104*(B4), 7055–7065. https://doi.org/10.1029/1998jb900111
Schmeling, H. (1986). Numerical models on the influence of partial melt on elastic, anelastic and electrical properties of rocks. Part II: electrical conductivity. *Physics of the Earth and Planetary Interiors*, *43*(2), 123–136. https://doi.org/10.1016/0031-9201(86)90080-4
Schwalenberg, K., Rath, V., & Haak, V. (2002). Sensitivity studies applied to a two-dimensional resistivity model from the Central Andes. *Geophysical Journal International*, *150*(3), 673–686. https://doi.org/10.1046/j.1365-246X.2002.01734.
Shimakawa, Y., & Honkura, Y. (1991). Electrical conductivity structure Beneath the Ryukyu trench-arc system and its relation to the subduction of the Philippine Sea plate. *Journal of Geomagnetism and Geoelectricity*, *43*(1), 1–20. https://doi.org/10.5636/jgg.43.1
Shimojuku, A., Yoshino, T., Yamazaki, D., & Okudaira, T. (2012). Electrical conductivity of fluid-bearing quartzite under lower crustal conditions. *Physics of the Earth and Planetary Interiors*, *198–199*, 1–8. https://doi.org/10.1016/j.pepi.2012.03.007
Shimojuku, A., Yoshino, T., & Yamazaki, D. (2014). Electrical conductivity of brine-bearing

quartzite at 1 GPa: Implications for fluid content and salinity of the crust. *Earth, Planets and Space*, *66*(1). https://doi.org/10.1186/1880-5981-66-2

Soyer, W., & Unsworth, M. (2006). Deep electrical structure of the northern Cascadia (British Columbia, Canada) subduction zone: Implications for the distribution of fluids. *Geology*, *34*(1), 53–56. https://doi.org/10.1130/G21951.1

Sun, W., Dai, L., Li, H., Hu, H., Jiang, J., & Wang, M. (2020). Electrical Conductivity of Clinopyroxene–NaCl–H_2–O System at High Temperatures and Pressures: Implications for High-Conductivity Anomalies in the Deep Crust and Subduction Zone . *Journal of Geophysical Research: Solid Earth*, *125*(4). https://doi.org/10.1029/2019jb019093

Syracuse, E. M., van Keken, P. E., Abers, G. A., Suetsugu, D., Bina, C., Inoue, T., et al. (2010). The global range of subduction zone thermal models. *Physics of the Earth and Planetary Interiors*, *183*(1–2), 73–90. https://doi.org/10.1016/j.pepi.2010.02.004

Tatsumi, Y. (1986). Formation of the volcanic front in subduction zones. *Geophysical Research Letters*, *13*(8), 717–720. https://doi.org/10.1029/GL013i008p00717

ten Grotenhuis, S. M., Drury, M. R., Spiers, C. J., & Peach, C. J. (2005). Melt distribution in olivine rocks based on electrical conductivity measurements. *Journal of Geophysical Research: Solid Earth*, *110*(12), 1–11. https://doi.org/10.1029/2004JB003462

Tiraboschi, C., Tumiati, S., Sverjensky, D., Pettke, T., Ulmer, P., & Poli, S. (2018). Experimental determination of magnesia and silica solubilities in graphite-saturated and redox-buffered high-pressure COH fluids in equilibrium with forsterite + enstatite and magnesite + enstatite. *Contributions to Mineralogy and Petrology*, *173*(1). https://doi.org/10.1007/s00410-017-1427-0

Uesugi, K., Tsuchiyama, A., Nakano, T., Suzuki, Y., Yagi, N., Umetani, K., & Kohmura, Y. (1999). <title>Development of microtomography imaging system for rock and mineral samples</title> In U. Bonse (Ed.) (pp. 214–221). https://doi.org/10.1117/12.363724

Uesugi, K., Suzuki, Y., Yagi, N., Tsuchiyama, A., & Nakano, T. (2001). Development of high spatial resolution X-ray CT system at BL47XU in SPring-8. *Nuclear Instruments and Methods in Physics Research Section A: Accelerators, Spectrometers, Detectors and Associated Equipment*, *467–468*, 853–856. https://doi.org/10.1016/S0168-9002(01)00491-0

van Keken, P. E., Hacker, B. R., Syracuse, E. M., & Abers, G. A. (2011). Subduction factory: 4. Depth-dependent flux of H_2O from subducting slabs worldwide. *Journal of Geophysical Research*, *116*(B1), B01401. https://doi.org/10.1029/2010JB007922

von Bargen, N., & Waff, H. S. (1986). Permeabilities, interfacial areas and curvatures of partially molten systems: Results of numerical computations of equilibrium microstructures. *Journal of Geophysical Research: Solid Earth*, *91*(B9), 9261–9276. https://doi.org/10.1029/JB091IB09P09261@10.1002/(ISSN)2169-9356.PARTMELT1

Waff, H. S. (1974). Theoretical considerations of electrical conductivity in a partially molten mantle and implications for geothermometry. *Journal of Geophysical Research*, *79*(26), 4003–4010. https://doi.org/10.1029/jb079i026p04003

Wang, D., Mookherjee, M., Xu, Y., & Karato, S. (2006). The effect of water on the electrical conductivity of olivine. *Nature*, *443*(7114), 977–980. https://doi.org/10.1038/nature05256

Wannamaker, P. E., Jiracek, G. R., Stodt, J. A., Caldwell, T. G., Gonzalez, V. M., McKnight, J. D., & Porter, A. D. (2002). Fluid generation and pathways beneath an active compressional orogen, the New Zealand Southern Alps, inferred from magnetotelluric data. *Journal of Geophysical Research*, *107*(B6), 2117. https://doi.org/10.1029/2001JB000186

Wannamaker, P. E., Grant Caldwell, T., Jiracek, G. R., Maris, V., Hill, G. J., Ogawa, Y., et al. (2009). LETTERS Fluid and deformation regime of an advancing subduction system at Marlborough, New Zealand. *Nature*. https://doi.org/10.1038/nature08204

Wannamaker, P. E., Evans, R. L., Bedrosian, P. A., Unsworth, M. J., Maris, V., & McGary, R. S. (2014). Segmentation of plate coupling, fate of subduction fluids, and modes of arc magmatism in Cascadia, inferred from magnetotelluric resistivity. *Geochemistry, Geophysics, Geosystems*, *15*(11), 4230–4253. https://doi.org/10.1002/2014GC005509

Wark, D. A., & Watson, E. B. (2000). Effect of grain size on the distribution and transport of deep-seated fluids and melts. *Geophysical Research Letters*, *27*(14), 2029–2032. https://doi.org/10.1029/2000GL011503

Watanabe, T., & Peach, C. J. (2002). Electrical impedance measurement of plastically deforming

halite rocks at 125 °C and 50 MPa. *Journal of Geophysical Research: Solid Earth*, *107*(B1), ECV 2-1-ECV 2-12. https://doi.org/10.1029/2001jb000204

Watson, E., & Brenan, J. M. (1987). Fluids in the lithosphere, 1. Experimentally-determined wetting characteristics of CO_2–H_2O fluids and their implications for fluid transport, host-rock physical properties, and fluid inclusion formation. *Earth and Planetary Science Letters*, *85*(4), 497–515. https://doi.org/10.1016/0012-821X(87)90144-0

Worzewski, T., Jegen, M., Kopp, H., Brasse, H., & Taylor Castillo, W. (2011). Magnetotelluric image of the fluid cycle in the Costa Rican subduction zone. *Nature Geoscience*, *4*(2), 108–111. https://doi.org/10.1038/ngeo1041

Yoshino, T., & Katsura, T. (2013). Electrical Conductivity of Mantle Minerals: Role of Water in Conductivity Anomalies. *Annual Review of Earth and Planetary Sciences*, *41*(1), 605–628. https://doi.org/10.1146/annurev-earth-050212-124022

Yoshino, T., Nishihara, Y., & Karato, S. I. (2007). Complete wetting of olivine grain boundaries by a hydrous melt near the mantle transition zone. *Earth and Planetary Science Letters*, *256*(3–4), 466–472. https://doi.org/10.1016/j.epsl.2007.02.002

Yoshino, T., Zhang, B., Rhymer, B., Zhao, C., & Fei, H. (2017). Pressure dependence of electrical conductivity in forsterite. *Journal of Geophysical Research: Solid Earth*, *122*(1), 158–171. https://doi.org/10.1002/2016JB013555